

Cite this: *Lab Chip*, 2014, **14**, 979

Switchable pH actuators and 3D integrated salt bridges as new strategies for reconfigurable microfluidic free-flow electrophoretic separation

Li-Jing Cheng^{*a} and Hsueh-Chia Chang^b

We present novel strategies for reconfigurable, high-throughput microfluidic free-flow electrophoretic separation using electrically switchable pH actuators and 3D integrated salt bridges to allow rapid formation of stable pH gradients and efficient electrophoresis. The pH actuator is achieved by microfluidic integration of bipolar membranes which change electrolyte pH by injecting excess H^+ or OH^- ions produced by a field-enhanced water dissociation phenomenon at the membrane junction upon voltage bias. The technique does not require conventional multiple buffer inflows and leaves no gas production as experienced in electrolysis, thus providing stable pH gradients for isoelectric focusing (IEF) separation. With the pH actuator inactivated, the platform can perform zone electrophoretic (ZE) separation in a medium of constant pH. We also describe the use of 3D integrated ion conductive polymers that serve as salt bridges for improving the voltage efficiency of electrophoresis and to allow high throughput. The proof of concept was successfully demonstrated for free-flow IEF and ZE separation of protein mixtures showing the potential and the simplicity of the platform for high-throughput and high-precision sample separation.

Received 5th September 2013,
Accepted 11th December 2013

DOI: 10.1039/c3lc51023a

www.rsc.org/loc

Introduction

Microfluidic free-flow electrophoresis (FFE) is a versatile and rapid technique for separation of proteins, organic compounds, and even cells based on their net charge.^{1–4} In this technique, samples are separated continuously by an electric field perpendicular to a pressure-driven electrolyte flow.^{5,6} Unlike other separation methods (*e.g.*, chromatography and gel electrophoresis) that require large sample volume and repeated sample loading, microfluidic FFE can handle samples in volumes as small as a few nanoliters and process the entire sample continuously in a high throughput flow, therefore saving considerable time and labour. With a pH gradient established in the separation medium, FFE works in an isoelectric focusing mode (FF-IEF) which separates molecules by differences in their isoelectric point (*pI*). In another mode with a medium of constant pH, the FFE setup performs free-flow electrophoresis (FF-ZE) capable of separating molecules according to their charge to size ratio.

FF-IEF is based on the formation of a stable pH gradient in the separation medium. Generation of a robust, linear pH gradient perpendicular to a flow direction is always

challenging in FF-IEF. Conventional large-scale FF-IEF systems use several inlets to fill the separation chamber with preseparated ampholytes that cover a pH range of 2.5 to 11.5. In miniaturized FF-IEF devices, the pH gradient can be established by introducing acid and base solution inflows,^{7,8} diffusing acid and base buffers through sidewall salt bridges,^{9–13} or changing local pH by electrolysis of water using embedded electrodes.^{14–16} The addition of different pH solutions requires complex flow control because of transient back pressures that can build up in a multi-inlet/outlet system.^{17,18} Moreover, due to the low electrolyte diffusivity, the desired pH gradient may not form rapidly. On the other hand, electrolysis of water produces hydrogen and oxygen bubbles that tend to interfere with microfluidic flow and require careful microfluidic design for their removal.¹⁹ Galvanic processes could also potentially create other electrochemical reaction products and contaminate the sample. To overcome these issues, we propose to generate pH gradients in microfluidic devices by taking advantage of field-enhanced water dissociation by bipolar membranes. The bipolar membrane is a bilayer membrane consisting of a cation exchange layer and an anion exchange layer. Under a reverse voltage bias, in which the anion exchange side connects to the positive potential, an ion depletion region with a thickness of a few Debye lengths forms at the junction of the two ion-exchange layers. With almost the entire applied voltage drop across this short distance, a significant electric field on

^a School of Electrical Engineering and Computer Science, Oregon State University, OR 97331, USA. E-mail: chengli@eecs.oregonstate.edu

^b Department of Chemical and Biomolecular Engineering, University of Notre Dame, IN 46556, USA

the order of as high as a few MV cm^{-1} can be created.^{20,21} Water molecules experiencing such a large electric field at the membrane junction are directly stripped apart into H^+ and OH^- ions based on electric field enhanced water dissociation.^{22–25} According to Onsager's theory of the second Wien effect, this phenomenon occurs due to the fact that the water dissociation rate constant increases with a strong electric field while the recombination rate does not.²⁶ Without any electron-transfer reaction that generates gas products, field-enhanced water dissociation produces H^+ and OH^- ions more efficiently than electrolysis of water.

The proposed microfluidic FFE platform comprises an upstream pH actuator and a downstream electrophoretic separation channel as shown in Fig. 1(a). The pH actuator is developed on the basis of our previous work²⁷ but with improvements in microfluidic design and membrane materials that offer faster, more stable pH control with lower voltage consumption. The device is configured by a microfluidic channel wedged between two bipolar membranes placed back-to-front to enable injection of H^+ and OH^- ions from different sides. With the pH actuator switched off, the electrolyte medium maintains a constant pH allowing the platform to perform FF-ZE (Fig. 1(b)). When switched on, the device alters the pH profile of the upstream electrolyte laminar flow by doping with H^+ and OH^- ions and forms a stable pH gradient in a downstream channel for FF-IEF as illustrated in Fig. 1(c). The function of the pH actuator is depicted in Fig. 1(d). The switchable pH actuation grants the reconfigurability of the platform, enabling dual-mode operation without changing electrolyte media.

Another issue that limits the production of reliable FFE is associated with the inability to create conductive electrical

connections for electrophoresis while avoiding the interference of electrolytic bubbles generated at electrodes. Here we introduce a novel technique that utilizes 3D integration of ion conductive polymers as salt bridges in PDMS microfluidic devices. The salt bridges conduct ions between a separation channel and electrodes while preventing bubbles from entering the separation region or any mixture of solution between the separated cells resulting from hydrostatic forces. The utility of salt bridges for FFE has been implemented *via* acrylamide-based hydrogel membranes^{7,9–12} and microchannel arrays.^{28,29} However, these hydrogel membranes have limited stability in extreme pH conditions and insufficient mechanical strength to withstand high flow rate. On the other hand, the microchannel arrays exhibit low electrical conductance; less than 5% of the applied voltage was reported to contribute to separation.²⁸ With such low voltage efficiency, the device has to operate at kilovolt ranges to carry out electrophoresis. The integrated 3D polymer salt bridges demonstrated here are employed to overcome these issues. The ion conductive composite is a Durapore membrane backbone encapsulated by a photocured interlocking polymer network. The polymer consists of long-chain aliphatic zpolyurethane and polyethyl glycol, which form a hard but flexible matrix as a structural support, and hydrophilic monomers and charged monomers which uptake water and offer ion conductivity. Apart from the material property, the 3D connection provides space for thicker ion conducting cross-section that improves ion conductance. Separation of protein mixtures in FF-IEF and FF-ZE modes was successfully demonstrated using this reconfigurable platform. The integration of these membrane microfluidic technologies was validated to allow for stable and precise separation.

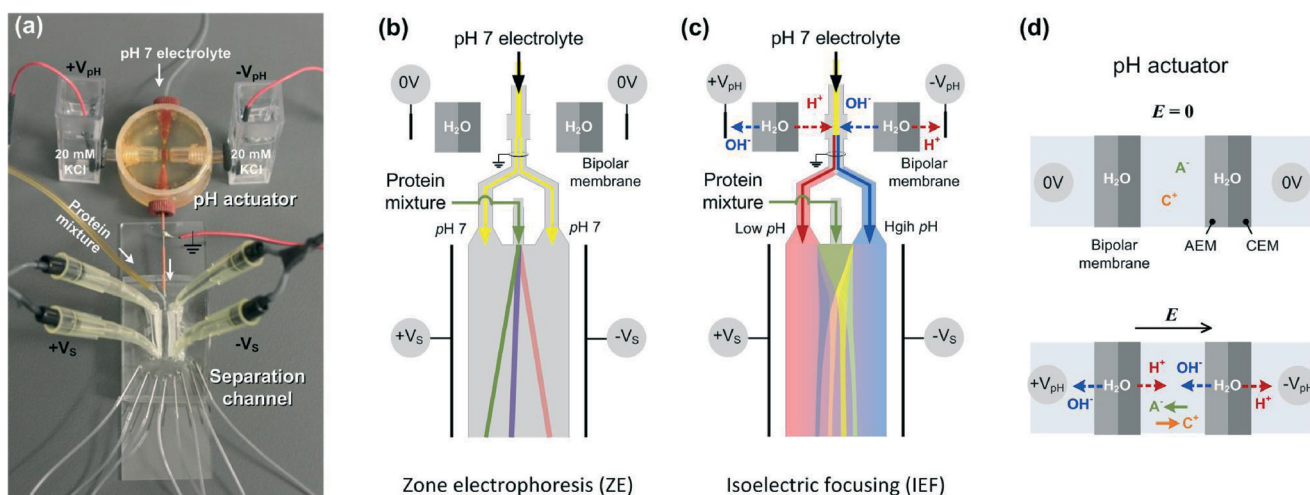


Fig. 1 (a) Image of a microfluidic free-flow electrophoresis platform composed of an upstream electrically switchable pH actuator and a downstream salt bridge-integrated separation channel. The switchable pH actuation provides reconfigurability of the platform for dual-mode operation—it produces a constant neutral pH medium for zone electrophoresis (b) or a pH gradient for isoelectric focusing (c). (d) The function of the pH actuator is based on an electric field enhanced water dissociation phenomenon in the integrated bipolar membranes upon voltage bias. The process dopes electrolyte microflows with excess H^+/OH^- ions and redistributes the existing cations (C^+) and anions (A^-) in the solution, resulting in a two-layer laminar flow containing a low-pH flow in one half and a high-pH flow in the other half. A symmetric voltage arrangement was employed for both upstream pH actuation ($\pm V_{\text{pH}}$) and downstream electrophoresis ($\pm V_s$) to avoid electrical crosstalk.

Experimental

Materials and reagents

Chemicals for device fabrication, including diallyldimethylammonium chloride solution (DADMAC, anion exchange monomer, 65 wt.% in H₂O), 2-acrylamido-2-methyl-1-propanesulfonic acid sodium salt solution (AMPSA, cation exchange monomer, 50 wt.% in H₂O), 2-hydroxyethyl methacrylate (HEMA), poly(ethylene glycol) diacrylate (PEGDA, Mn 700), trichloro(1H,1H,2H,2H-perfluorooctyl)silane (perfluorosilane) and 2-hydroxy-4'-(2-hydroxyethoxy)-2-methylpropiophenone (photoinitiator), were purchased from Sigma-Aldrich; aliphatic urethane acrylate solution (m.w. 2000, 50% in water) was kindly provided by CYTEC; Durapore membrane (VVP) was purchased from Millipore. Bipolar membrane, Neosepta BP-1 (ASTOM Corp.), was obtained from Ameridia. Poly(dimethyl siloxane) (PDMS, Sylgard 148) was from Dow Corning. Hydrion pH indicator solution (UI-100) was from Micro Essential Lab. Assay reagents, namely, monobasic sodium phosphate, dibasic sodium phosphate, (hydroxypropyl)methyl cellulose (HPMC), poly(vinyl alcohol) (PVA, m.w. 130k), phosphate-buffered saline (PBS) and Nonident P-40 substitute (NP-40), were purchased from Sigma-Aldrich; carrier ampholyte SERVALYT™ 2-11 was from Biophoretics. Fluorophore conjugated proteins, including Alexa 594-conjugated ovalbumin, Alexa 350-conjugated neutravidin, Alexa 488-conjugated wheat germ agglutinin and Alexa 488-conjugated avidin, were purchased from Invitrogen.

Device design and fabrication

The pH actuator was designed to have a H⁺/OH⁻ ion injection region formed by a 1 mm-diameter, 400 μm-thick disk-shaped chamber enclosed by two bipolar membranes located midway of a 250 μm-wide cylindrical channel. The bipolar membranes separate the microfluidic channel and two electrode reservoirs. The microfluidic part was fabricated by casting UV-curable polyurethane-based prepolymer on a mould constructed by an assembly of tubings and connectors. The bipolar membrane was assembled to enclose one end of the tube to allow electrolyte connection while preventing any across-membrane leakage. Two bipolar membrane-sealed tubes with different ion-exchange sides facing outward were then inserted into the device. Once filled with electrolyte, the membranes allow ion conduction devoid of fluidic flow.

The downstream free-flow electrophoresis (FFE) device was a 1.8 mm wide, 14 mm long, 35 μm thick PDMS microfluidic channel with two inlets (one for sample flow and one for pH flow), multiple outlets and two polymer salt bridges that interface the channel to electrolyte reservoirs from both sides. The microfluidic design manipulated the two inflows such that the pH flow bifurcated and hydrodynamically focused the sample flow injected from the centre. The pH flow inlet was connected to the microfluidic channel at a 45 degree angle to prevent any vortices resulting from the sharp turn that corrupt the pH profile. The electrode reservoirs made of polyurethane tubes along with polymer salt bridges

were embedded in the PDMS device to establish ion conduction between the separation channel and external Ag/AgCl electrodes through vertical pathways. Cation exchange material (CEM) and anion exchange material (AEM) were adapted as salt bridges connecting to different sides of the channel. To ensure proper operation of FF-IEF, CEM was arranged to contact the low-pH sheath flow and connect to the anode.

The FFE device with embedded salt bridges was fabricated using a novel technique that combines soft lithography and photo-polymerization of ion conductive polymers. In brief, a SU-8 mould for PDMS microfluidic devices was fabricated on a silicon substrate using photolithography. The mould surface was oxygen plasma treated and functionalised with hydrophobic perfluorosilane to facilitate the demoulding process. As illustrated in Fig. 2(a–e), the embedded 3D salt bridges in PDMS devices were fabricated by mounting membrane subunits on the mould followed by PDMS casting. The membrane subunit was formed by an enclosed tubing as an electrode reservoir, two through holes on top for fluidic connection and a slit cut for inserting a hydrophilic Durapore membrane. The Durapore membrane connected reservoir tube was placed to align with the ridge of the channel mould pattern and was then soaked in ion conductive prepolymer. The prepolymer for AEM was composed of a mixture of 7% v/v DADMAC monomer solution, 15% v/v HEMA, 18% v/v deionized (DI) water, 25% v/v PEGDA, 35% v/v aqueous aliphatic polyurethane acrylate solution and an additional 2% w/v photoinitiator. A similar composition was prepared for CEM except that the monomer solution was replaced by 13% v/v AMPSA and the DI water lowered to 15% v/v. The charged monomer concentrations in both membranes were equivalent to about 300 mM and were assessed to yield 0.29 mS cm⁻¹ of ion conductivity after polymerization. The success of this fabrication process resulted from the fact that the prepolymer solutions tend to stay in hydrophilic Durapore membranes but dewet on the hydrophobic mould surfaces; the large meniscus–mould contact angle allows the membranes to attach to the mould pattern through the prepolymer solutions with small contact areas. After UV exposure under a nitrogen atmosphere, the cured polymer formed flexible ion conductive materials that encapsulated the Durapore membrane and secured the membrane subunits on the mould surface. The polymerized ion conductive membranes were measured to be about 400 μm thick and 1 mm long. A PDMS mixture in the ratio of 10:1 by weight of base and curing agent was poured on the mould which had membrane-subunits attached on top. After curing, the PDMS device as well as the embedded membrane subunits were demoulded. The membrane-integrated PDMS devices were punched to form fluid connections and treated with oxygen plasma prior to permanently bonding to a glass slide. The device was filled with an aqueous solution containing 50 mM KCl and 3% PVA overnight before use. Fig. 2(f) and (g) show the top view and cross-section view images of the resulting separation device which includes embedded salt bridges connecting alongside the microfluidic

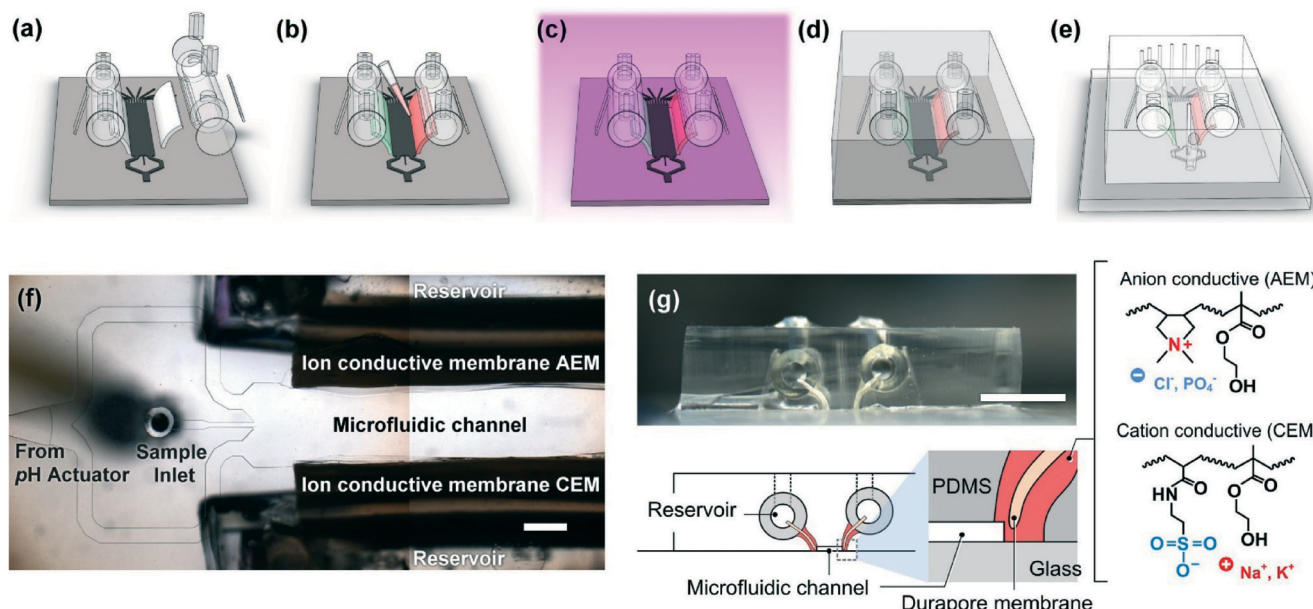


Fig. 2 Schematic illustration corresponding to steps for fabricating a 3D salt bridge-integrated microfluidic device: (a) assembly of membrane subunits consisting of electrode reservoirs and Durapore membranes, and placement of the membrane subunits on a surface-fluorinated SU-8 mould; (b) application of UV-curable ion-conductive prepolymer on the Durapore membranes; (c) UV polymerization under a nitrogen atmosphere; (d) PDMS casting; and (e) hole punching and plasma bonding on a glass substrate. (f) Top view optical image of the resulting separation device. Scale bar represents 1 mm. (g) Cross-section optical image and schematic of the device. The inset details the structure of the channel–salt bridge interface and the representative chemical structures involved in the ion-conductive polymers. Anion exchange membrane (AEM) and cation exchange membrane (CEM) were based on chemicals containing quaternary ammonium groups and sulfonate groups, respectively. Polyethyl glycol and polyurethane crosslinker are not shown here. Scale bar represents 5 mm.

channel. The final channel width defined by the distance between the two membrane salt bridges was measured to be about 1.6 mm. The illustration details the structure of the membrane–channel interface and the chemical groups involved in the ion conductive materials.

Experimental setup

The pH actuator was connected upstream to a syringe pump and downstream to the FFE separation chip *via* a PEEK tubing intersected by a segment of stainless tubing which was wired to electrical ground. The syringe pump supplied pH neutral electrolyte, *i.e.*, a mixture of 20 mM KCl solution and 50 mM pH 7 phosphate electrolyte prepared with mono-basic sodium phosphate and di-basic sodium phosphate. Two bipolar membrane-sealed tubes were filled with 20 mM KCl solution and mounted to the device to interface the electrolyte flow. Typical voltages ($\pm V_{\text{pH}}$) of about ± 4.2 V were applied across the bipolar membranes through platinum electrodes with anode connecting to the anion-exchange side to trigger field enhanced water dissociation. Voltages ($\pm V_s$) ranging from ± 20 V to ± 60 V were applied across the separation channel to generate electrophoresis.

Symmetric voltages were assigned across both pH actuator ($\pm V_{\text{pH}}$) and separation channel ($\pm V_s$) to create a virtual ground along the centre axis of the entire microfluidic system. Such a symmetric voltage arrangement combined with a real electric ground between the upstream pH actuator and the

downstream separation channel bypassed any electrical crosstalk between these two components. Without the symmetric setup, the device cannot operate properly and the high voltage crosstalk could damage the bipolar membranes.

A mixture of 40% Hydrion pH indicator solution in 50 mM pH 7 phosphate buffers was utilized to visualize the pH profiles of the solutions in the device. Protein separation was observed by imaging a mixture of fluorophore-conjugated protein sample prepared in the solution containing a final concentration of 1× PBS, 0.2% HPMC, 0.2% NP-40 and additional 3% Servalyte for FF-IEF. The protein mixture for ZE separation contained two different protein samples, including 100 $\mu\text{g ml}^{-1}$ ovalbumin-Alexa 594 and 60 $\mu\text{g ml}^{-1}$ avidin-Alexa 488. Two additional proteins, 120 $\mu\text{g ml}^{-1}$ neutravidin-Alexa 350 and 150 $\mu\text{g ml}^{-1}$ wheat germ agglutinin-Alexa 488, were included for IEF separation. Bright-field and fluorescence images were captured by QCapture Pro 7 software using an Olympus microscope (IX71) equipped with fluorescence filter sets and a colour CCD camera (Retiga 2000R). Quantification of fluorescence images, fluorescence background subtraction and image overlay were carried out using ImageJ software.

Results and discussion

pH actuator

In our previous work, we have successfully demonstrated pH actuation in planar microfluidic devices using synthesized

bipolar membranes.²⁷ The device was capable of generating various constant pH and pH gradients by means of electrical control. However, the prior design suffered from low ion conductance because of the thin channel height and small ion injection cross-sections. Most of the applied voltage dropped across the channels rather than across the bipolar membranes. As a result, a high voltage greater than 50 V was required to initiate field-enhanced water dissociation. Moreover, the two bipolar membranes were located relatively far away across the channel from each other. An operating condition of small electric field or high flow rate could hinder the injected H⁺/OH⁻ ions from reaching the centre of the flow. The resulting pH actuation became less efficient and was sensitive to flow rate.

To reduce operating voltage and improve H⁺/OH⁻ doping efficiency, the new pH actuator was designed to have a wide ion injection cross-section while retaining the rest of the channel small, forming a thin disk-shaped flow chamber enclosed by bipolar membranes. The unique channel geometry offered several advantages over the previous planar design. First, it presented much larger contact areas for bipolar membranes (BP-1) which considerably increase ion conductance across the membranes and hence lower the operating voltage. In addition, the enlarged volume in the pH actuation region allowed a high throughput at low electrolyte velocity and a higher H⁺/OH⁻ ion injection rate per unit volume. The lower Peclet number, based on channel height, the electrolyte velocity and the H⁺/OH⁻ diffusivity, implies more time for electrolyte ion equilibration by the transverse electric field and neutralization of the injected H⁺/OH⁻ ions (see illustration in Fig. 1). The reduced electrolyte flow velocity also minimized the deflection of ion injection which enabled effective ion doping over the entire inflow. Overall, the current design produced more efficient and robust pH actuation.

The optical image of the pH actuator in Fig. 3(a) shows the resulting pH actuation by visualizing the colour change of the indicator-containing solution throughout the device. The pH neutral electrolyte solution (yellow colour) was introduced from the top and turned into a two-layer laminar flow with different colours (red and blue) after passing through the ion doping region in the middle of the device. The colour change indicates that the solution was doped to a high pH (about pH 11) in the right half of the outflow and a low pH (about pH 2) in the other half. The result was observed under an operating voltage of 4.2 V ($\pm V_{\text{pH}} = \pm 4.2$ V) which yielded a current of about 0.22 mA (equivalent current density of 28 mA cm⁻² for a 1 mm wide circular membrane). The operating voltage was beyond the onset voltage required for field enhanced water dissociation as evidenced by the *I*-*V* characteristics of a reverse-biased bipolar membrane. The *I*-*V* curve in Fig. 3(c) measured in the presence of 20 mM KCl solution exhibits a typical low-current saturation region at low V_{pH} followed by a progressive increase in current with V_{pH} beyond 3 V due to the excess ion current contributed by enhanced water dissociation. The measured onset voltage is relatively higher than the data provided by the manufacturer and other works.³⁰ It could be attributed to the series resistance

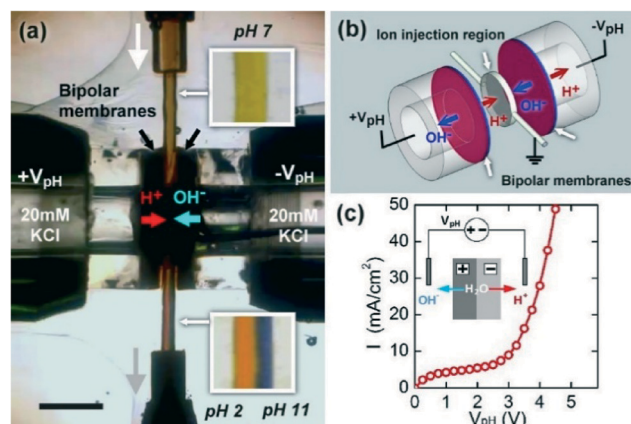


Fig. 3 (a) Microscopic image of an operating pH actuator which converts pH neutral electrolyte inflow into a two-layer laminar flow with low-pH in the left half and high-pH in the other half. The solution pH level was visualized by introducing an electrolyte containing pH indicator, 50 mM pH 7 phosphate buffer and 20 mM KCl. Voltages of ± 4.2 V were applied across two bipolar membranes through electrode reservoirs which contained 20 mM KCl solution. (b) Exploded illustration details the function of the pH actuator which adjusts solution pH by doping with H⁺/OH⁻ ions when the flow passes through the ion injection region, i.e., the disk-shaped chamber sandwiched between two bipolar membranes. (c) Measured *I*-*V* characteristic of an individual bipolar membrane shows a significant increase in ion current due to electric field-enhanced water dissociation with an applied voltage greater than 3 V. Scale bar represents 1 mm.

contributed by the device structure and the relatively low electrolyte concentration. The measured ion current of 0.22 mA during operation yields a H⁺/OH⁻ production rate of 1.38×10^{15} s⁻¹ in the ion injection region. With this ion injection rate, the pass-through electrolyte, introduced at a typical flow rate of 12 $\mu\text{l s}^{-1}$, can be doped to H⁺/OH⁻ concentrations of 0.011 M, forming pH 2 and pH 12 solutions. The calculated result agrees with the experimental observation of the solution pH shown in Fig. 3(a). The resulting pH profile was insensitive to the electrolyte flow rate—the pH profile can withstand a flow rate up to 60 $\mu\text{l min}^{-1}$, much higher than the typical values required for FFE. The switching response of the pH actuation was shorter than 1 second, much faster than that of the old design which took a few to 10 seconds to respond depending on applied voltage. The fast transient response was the consequence of the high ion conductance in both microfluidic device and membranes. The device was found to be very robust and the results were highly reproducible. The same device functioned properly at least for four months. The only failures observed were those with impaired sealing to the reservoir tubes. Unlike the hydrogel-based bipolar membranes in our previous design which requires being wet all the time to function properly, BP-1 managed to recover its function by rewetting after being dry for a few days.

3D integration of ion conductive membranes as salt bridges for separation devices

As shown in Fig. 4(a), the pH profile established in the separation channel can be visualized by using pH indicator-containing

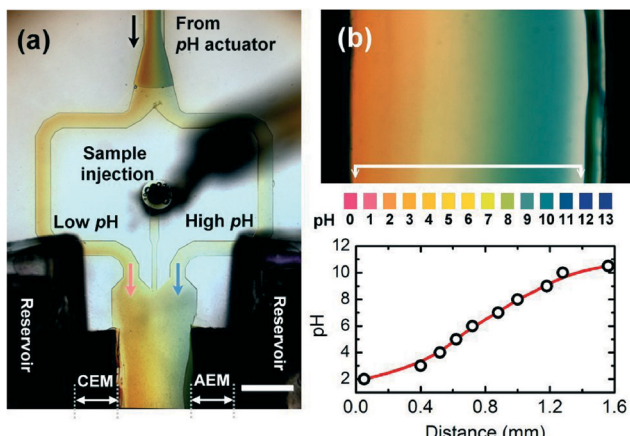


Fig. 4 pH profiles in the separation channel. (a) The pH-actuated flow bifurcated into a low-pH branch in the left side and a high-pH branch in the right side, hydrodynamically focused the sample stream injected in the centre, and formed a pH gradient across the entire separation channel. (b) An almost linear pH gradient was visualized by using pH indicator-containing solutions. The pH profile was estimated and summarized in the plot based on the colour chart.

solution. The colour distribution in the flow indicated that the pH-actuated two-layer laminar inflow first bifurcated into a high-pH and a low-pH branch and hydrodynamically focused a sample flow injected through a centre inlet. The two pH flows established a lateral pH gradient throughout the separation channel by diffusion and meantime provided sheath flows preventing analyte from traversing into the salt bridges alongside the channel. The pH gradient developed quickly within 2 mm away from the inlets and became optimal for separation after 4 mm. Fig. 4(b) shows a pH gradient building up 8 mm away from the channel inlets with a pH-actuated flow at $12 \mu\text{l min}^{-1}$ and a pH 7 analyte flow at $5 \mu\text{l min}^{-1}$. The pH profile was evaluated according to the colour distribution of the indicator-containing solution and summarized in the following plot. A wide-range pH gradient was achieved to cover approximately from pH 2 to pH 10 with an almost linear gradient of 7.6 pH mm^{-1} in the middle of the channel. It is also worth mentioning that the pH gradient was observed under a voltage bias of 70 V ($\pm V_s = \pm 35 \text{ V}$) across the separation channel with the positive polarity on the CEM side. No significant effect on the pH profile was found except that the pH indicator near the AEM was slightly depleted as shown in the whitened area at the right edge. The result could be due to the influence of electrophoretic force on the negatively charged pH dyes.

Another unique feature of the electrophoretic separation device is its out-of-plane salt bridge connections between the planar microfluidic channel and the elevated electrode reservoirs. The presented new design improved the microfluidic salt bridges in several aspects. First, the salt bridges were fabricated to be more durable owing to the use of porous hydrophilic Durapore membranes and long-chain aliphatic polyurethane as a crosslinker that strengthens physical supports. The materials provided flexibility as well as mechanical strength whilst maintaining the required water

uptake. In addition, the conventional salt bridges in microfluidic systems usually have their size restricted by the microfluidic channel height.³¹ The 3D configuration, however, can accommodate thick ion conductive cross-sections which improve overall ion conductance. To estimate the ion conductance of the integrated salt bridge R_{SB} (1.5 mm long, 12 mm wide, and 400 μm thick), we measured the current of a dummy device with a stand-alone salt bridge (3 mm long, 12 mm wide, and 400 μm thick), twice as long as the integrated counterpart, in connection with two reservoir tubes containing 50 mM and pH 7 phosphate buffer solutions. A resistance of $32.2 \text{ k}\Omega$ on average was obtained which corresponds to a resistance of $R_{\text{SB}} = 16.1 \text{ k}\Omega$ for each salt bridge in the PDMS separation device. The result yields an ion conductivity of about $0.18\text{--}0.21 \text{ mS cm}^{-1}$ for both salt bridges based on anion and cation exchange membranes. The quantity is comparable to the theoretical estimation of 0.28 mS cm^{-1} based on the 300 mM charged monomer concentration in the polymer. Because the polymer composite contained a certain percentage of long-chain polymer which contributed to mechanical strength rather than to ion conduction, the resulting ion conductivity is lower than the hydrogel-based materials that gained its high conductivity from more than 90% of water uptake. Nevertheless, the loss of conductivity can be compensated by adding up the membrane cross-section that increases the final ion conductance. The total resistance across the separation device, including two salt bridges and the separation channel ($2R_{\text{SB}} + R_{\text{Ch}}$), was measured to be about $505 \text{ k}\Omega$ based on the ion current (0.13–0.15 mA) monitored during separation at 70 V . The measured resistances indicate that about 93% (*i.e.*, $R_{\text{Ch}}/(2R_{\text{SB}} + R_{\text{Ch}})$) of the applied voltage contributed to electrophoresis. The combination of new material composition and physical configuration grants the integrated salt bridge durability that hydrogel cannot achieve and high voltage efficiency comparable to the hydrogel-based counterparts.

Isoelectric focusing

Free flow isoelectric focusing was successfully demonstrated in the device by separating a mixture of four different fluorophore-labelled proteins which possess distinguished isoelectric points ranging from $\text{pI } 4.5$ to 10 . They are ovalbumin-Alexa 594 ($\text{pI } 4.5\text{--}4.8$), neutravidin-Alexa 350 ($\text{pI } \sim 6.3$), wheat germ agglutinin-Alexa 488 ($\text{pI } \sim 8.5$) and avidin-Alexa 488 ($\text{pI } \sim 10$). In the beginning of each separation experiment, both sample flow and pH-actuated flow were adjusted to form a hydrodynamically focused sample stream. The pH-actuated flow was produced in the absence of pH indicators under a typical voltage of $\pm V_{\text{pH}} = \pm 4.2 \text{ V}$ and was introduced to the separation channel at a flow rate of $12 \mu\text{l min}^{-1}$. The sample flow was simultaneously injected at a flow rate of $5 \mu\text{l min}^{-1}$. The resulting flow velocity was estimated to be about 5 mm s^{-1} . A voltage up to 110 V ($\pm V_s = \pm 55 \text{ V}$) was tested for separation. Vortex flow near the AEM salt bridge was found to launch at a voltage greater than 110 V , disturbing the laminar flow for separation. The overlaid fluorescence images in Fig. 5(a) and (b)

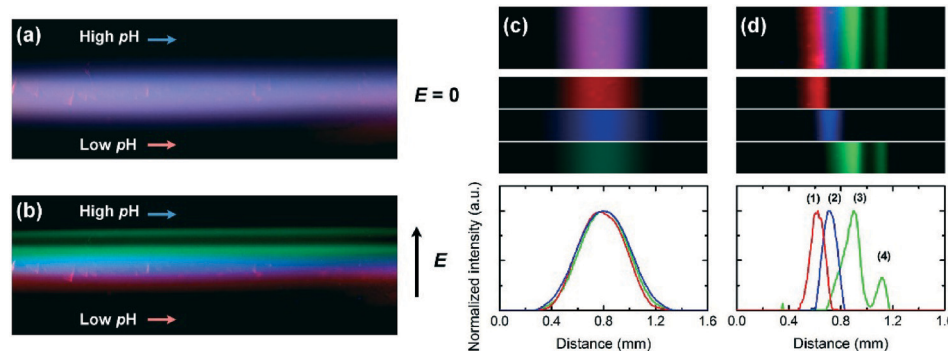


Fig. 5 Free-flow isoelectric focusing separation of four different fluorophore-conjugated proteins. Overlaid fluorescence images at zero electric field (a) and 390 V cm^{-1} (b) show that the protein mixture focused into separated streamlines according to their pIs under the applied electric field. The flow velocity was about 5 mm s^{-1} . (c) and (d) present the zoom-in details and the corresponding fluorescence intensity profiles of the sample streams before and after separation, respectively. The numbers labelled on the separated peaks correspond to the fluorophore conjugated protein samples under test: (1) ovalbumin-Alexa 594 ($\text{pI} \sim 4.5\text{--}4.8$, red), (2) neutravidin-Alexa 350 ($\text{pI} \sim 6.3$, blue), (3) wheat germ agglutinin-Alexa 488 ($\text{pI} \sim 8.5$, green) and (4) avidin-Alexa 488 ($\text{pI} \sim 10$, green).

show the sample mixture flow captured in the channel area covering a distance from 8 to 12 mm away from the inlets. It can be seen that at zero E -field ($\pm V_s = 0$; $\pm V_{\text{pH}} = \pm 4.2 \text{ V}$), all the sample streams exhibit identical dispersion profile due to diffusion. The single sample stream divides into distinguished analyte bands according to their pIs when a voltage of 70 V across the channel was applied ($\pm V_s = \pm 35 \text{ V}$; $\pm V_{\text{pH}} = \pm 4.2 \text{ V}$), which corresponds to an effective electric field of 390 V cm^{-1} . Separate fluorescence image layers and their intensity profiles are summarized in Fig. 5(c) and (d) to resolve the distribution of different protein streams across the channel. The fluorescence profiles indicate that the separate streams are located correspondingly to the pH distribution shown in Fig. 4(b). The low-concentrated avidin-Alexa 488 yields a narrow line width with standard deviation $\sigma = 34 \mu\text{m}$ ($\sigma = \text{fwhm}/2.35$) and is identified as peak (4) in the intensity profile of Fig. 5(d). Other separated streams with high initial concentrations have thicker line widths. The σ values of peaks (1), (2) and (3) in Fig. 5(d) are $53 \mu\text{m}$, $56 \mu\text{m}$ and $60 \mu\text{m}$, respectively. The results lead to a peak capacity of $n = 8$ in the 1.6 mm-wide channel based on the definition of $n = L/(4\sigma_{\text{av}})$, where L and σ_{av} are the total length of the pH gradient and the average of the four standard deviations, respectively.³² The separation result shows that the peak capacity is comparable to 7 peaks within 3 mm reported in ref. 33 and 8 peaks within 10 mm reported in ref. 2 but is inferior to the result presented in ref. 7 which has 22 peaks within 1.8 mm. Relatively high sample concentrations were employed in our experiment to achieve sufficient fluorescence intensity under wide-field and low-magnification imaging conditions. The thick focused bands for high concentration samples could result from coupling between longitudinal convection and non-uniform transverse concentration at the focused band. It is a concentration-dependent hydrodynamic dispersion mechanism because the focused solute can change the local pH and skew the transverse profile. It is hence a curious concentration-dependent convective mixing mechanism that is unique to free-flow isoelectric separation. Further study is required to quantify this unique dispersion mechanism.

Overall, the peak capacity of the IEF device is not high enough to satisfy high-resolution separation but could be sufficient for preparative separation.

Zone electrophoresis

Free-flow zone electrophoresis (FF-ZE) was performed in the same platform with the pH actuator switched off ($\pm V_{\text{pH}} = 0 \text{ V}$). Without pH actuation, the sheath flows supplied a pH 7 phosphate buffer, providing a uniform pH condition across the entire separation channel. We demonstrated FF-ZE by separating the mixture of cationic ovalbumin-Alexa 594 and anionic avidin-Alexa 488 at pH 7. Fig. 6 displays the separation result in a merged fluorescence image along the channel and the fluorescence intensity profiles captured at four different positions along the separation channel. The experiment was carried out with the sample flow rate being $4 \mu\text{l min}^{-1}$ and the sheath flow rate being $26 \mu\text{l min}^{-1}$ which determined the sample injection width of about $220 \mu\text{m}$ and yielded a flow velocity of about 15 mm s^{-1} . The FF-ZE separation was evidenced by the splitting sample streamline under an electric field of about 220 V cm^{-1} . The sample flow was initially hydrodynamically focused and separated into two branches that deflect into opposite directions due to the different charge polarities carried by these two proteins at neutral pH. The progression of separation and dispersion of the sample flows is resolved by their fluorescence intensity profiles at different distances away from the inlet. Different from the steady focused stream profiles observed in FF-IEF, the separated streams in FF-ZE keep migrating away from the original streamline all the way down to the outlets and display line width dispersion, indicating the effect of electrophoresis without electrofocusing property. In this demonstration, a peak capacity of only 5 peaks within 1.6 mm is obtained because the width of the injected sample stream already covers one-fifth of the channel width. Decrease of sample injection width is expected to reduce the band width dispersion and increase the peak capacity.⁶

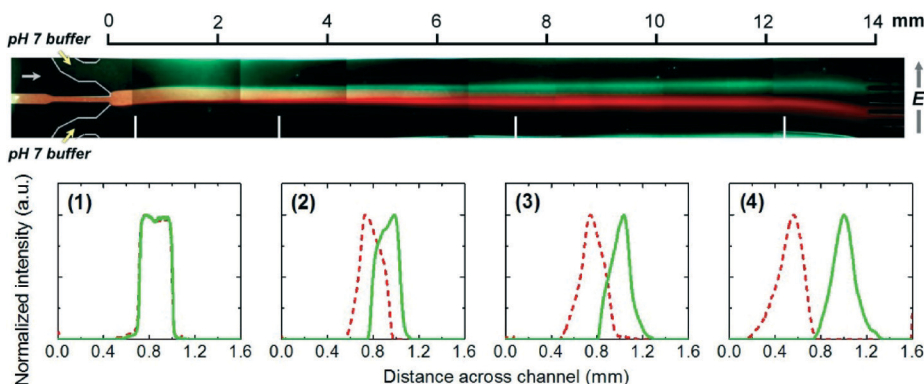


Fig. 6 Free-flow zone electrophoresis separation of a sample mixture containing cationic ovalbumin-Alexa 594 (red) and anionic avidin-Alexa 488 (green) in a pH neutral medium. The separation was performed at 220 V cm^{-1} with a flow velocity of about 15 mm s^{-1} . The fluorescence image reveals the continuous migration and dispersion of the sample streams down through the channel. The fluorescence intensity profiles at four different cross-sections along the channel are summarized to show the separation and dispersion processes.

Conclusions

Electrical pH actuation and 3D integration of ion conductive membranes were demonstrated to realize a reconfigurable microfluidic free-flow separation platform capable of FF-IEF and FF-ZE without changing medium inflows. The presented pH actuator adjusts pH levels in continuous-flow microfluidics by means of field-enhanced water dissociation. It uses voltage-biased bipolar membranes to split water molecules into H^+ / OH^- ions and relocate them to alter local pH in microfluidics. The device enabled rapid generation of pH gradients in a wide range from pH 2 to pH 10 without conventional multi-flow configuration, simplifying the overall flow control. In addition, we introduced polyurethane based salt bridges with 3D connection to provide higher ion conductance and endure higher pressure/flow rate. Although the 3D configuration was realized in PDMS devices, the approach could be simplified and applied to different substrate materials, providing an alternative option for microfluidic design. We presented the proof-of-concept demonstration of these new techniques in both FF-IEF and FF-ZE. Further optimization of parameters in separation conditions and microfluidic configuration could lead to high throughput, high resolution free-flow separation. With the current result, the platform can serve as a rapid sample preparation unit and potentially be integrated into downstream analytical tools such as mass spectroscopy to achieve on-line high-resolution molecule identification.

Acknowledgements

This work was supported by the Advanced Diagnostics and Therapeutics (AD&T) Initiative at the University of Notre Dame.

References

- D. E. Raymond, A. Manz and H. M. Widmer, *Anal. Chem.*, 1994, **66**, 2858–2865.
- D. E. Raymond, A. Manz and H. M. Widmer, *Anal. Chem.*, 1996, **68**, 2515–2522.
- M. Islinger, C. Eckerskorn and A. Völkl, *Electrophoresis*, 2010, **31**, 1754–1763.
- P. J. A. Weber, G. Weber, C. Eckerskorn, U. Schneider and A. Posch, *Handbook of Isoelectric Focusing and Proteomics*, 2005, 211245.
- D. Kohlheyer, J. C. T. Eijkel, A. van den Berg and R. B. M. Schasfoort, *Electrophoresis*, 2008, **29**, 977–993.
- R. T. Turgeon and M. T. Bowser, *Anal. Bioanal. Chem.*, 2009, **394**, 187–198.
- D. Kohlheyer, J. C. T. Eijkel, S. Schlautmann, A. van den Berg and R. B. M. Schasfoort, *Anal. Chem.*, 2007, **79**, 8190–8198.
- H. L. Lee, P. Boccazzini, R. J. Ram and A. J. Sinskey, *Lab Chip*, 2006, **6**, 1229–1235.
- J. Wen, J. W. Albrecht and K. F. Jensen, *Electrophoresis*, 2010, **31**, 1606–1614.
- J. Wen, E. W. Wilker, M. B. Yaffe and K. F. Jensen, *Anal. Chem.*, 2010, **82**, 1253–1260.
- J. W. Albrecht and K. F. Jensen, *Electrophoresis*, 2006, **27**, 4960–4969.
- J. W. Albrecht, J. El-Ali and K. F. Jensen, *Anal. Chem.*, 2007, **79**, 9364–9371.
- H. Chun, T. D. Chung and J. M. Ramsey, *Anal. Chem.*, 2010, **82**, 6287–6292.
- H. Corstjens, H. A. H. Billiet, J. Frank and K. C. A. M. Luyben, *Electrophoresis*, 1996, **17**, 137–143.
- K. Macounova, C. R. Cabrera, M. R. Holl and P. Yager, *Anal. Chem.*, 2000, **72**, 3745–3751.
- C. R. Cabrera, B. Finlayson and P. Yager, *Anal. Chem.*, 2001, **73**, 658–666.
- H. Suzuki and R. Yoneyama, *Sens. Actuators, B*, 2003, **96**, 38–45.
- H. Hosono, W. Satoh, M. Toya, K. Morimoto, J. Fukuda and H. Suzuki, *Sens. Actuators, B*, 2008, **132**, 614–622.
- S. Köhler a, C. Weilbeer, S. Howitz, H. Becker, V. Beushausen and D. Belder, *Lab Chip*, 2011, **11**, 309–314.
- H. Strathmann, J. J. Krol, H.-J. Rapp and G. Eigenberger, *J. Membr. Sci.*, 1997, **125**, 123–142.
- S. Mafé and P. Ramfrez, *Acta Polym.*, 1997, **48**, 234–250.

- 22 K. N. Mani, *J. Membr. Sci.*, 1991, **58**, 117–138.
- 23 I. C. Bassignana and H. Reiss, *J. Membr. Sci.*, 1983, **15**, 27–41.
- 24 G. Grossman, *J. Phys. Chem.*, 1976, **80**, 1616–1625.
- 25 R. Simons and G. Khanarian, *J. Membr. Sci.*, 1978, **38**, 11–30.
- 26 L. Onsager, *J. Chem. Phys.*, 1934, **2**, 599–615.
- 27 L.-J. Cheng and H. C. Chang, *Biomicrofluidics*, 2011, **5**, 046502–046508.
- 28 Y. Xu, C.-X. Zhang, D. Janasek and A. Manz, *Lab Chip*, 2003, **3**, 224–227.
- 29 D. Janasek, M. Schilling, J. Franzke and A. Manz, *Anal. Chem.*, 2006, **78**, 3815–3819.
- 30 A. Alcaraza, P. Ramírez, S. Mafé, H. Holdijk and B. Bauerd, *Polymer*, 2000, **41**, 6627–6634.
- 31 S. Park, T. D. Chung and H. C. Kim, *Microfluid. Nanofluid.*, 2009, **6**, 315–331.
- 32 Q. Wang, H. D. Tolley, D. A. LaFebre and M. L. Lee, *Anal. Bioanal. Chem.*, 2002, **373**, 125–135.
- 33 D. Kohlheyer, Geert A. J. Besselink, S. Schlautmann and R. B. M. Schasfoort, *Lab Chip*, 2006, **6**, 374–380.